Available online at www.sciencedirect.com
SCIENCE DIRECT®
Journal of Magnetic Resonance 167 (2004) 306–316
JMR Journal of Magnetic Resonance
www.elsevier.com/locate/jmr

$T_{1\rho}$-weighted MRI using a surface coil to transmit spin-lock pulses

Arijitt Borthakur,* Sridhar R. Charagundla, Andrew Wheaton, and Ravinder Reddy

Department of Radiology, University of Pennsylvania, Philadelphia, PA, USA

Received 29 July 2003; revised 8 January 2004

Abstract

$T_{1\rho}$-weighted MRI is a novel basis for generating tissue contrast. However, it suffers from sensitivity to B_1 inhomogeneity. First, excitation with a spatially varying B_1 causes flip-angle artifacts and second, spin locking with an inhomogeneous B_1 results in non-uniform $T_{1\rho}$ contrast. In this study, we overcome the former complication with a specially designed spin-locking pulse sequence and we successfully obtain $T_{1\rho}$-weighted images with a surface coil. In this pulse sequence, the spin-lock pulse was divided into segments of equal duration and alternating phase. This ''self-compensating'' $T_{1\rho}$-preparatory pulse sequence was analyzed and the effect of an inhomogeneous B_1 field was simulated using the Bloch equations. $T_{1\rho}$-weighted MR images of a phantom and a human knee joint in vivo were obtained on a clinical scanner with a surface coil to demonstrate the utility of the pulse sequence. The self-compensating $T_{1\rho}$-prepared pulses sequence resulted in substantially reduced image artifacts compared to the conventional, single-phase spin-lock pulse.

Keywords: $T_{1\rho}$; Spin-lock imaging; Image artifacts; Surface coil; Cartilage

1. Introduction

Traditional MR imaging has relied on T_1- and T_2-based image contrast to distinguish normal and pathological tissue. An alternative contrast mechanism is based on $T_{1\rho}$, the spin–lattice relaxation time in the rotating frame. In $T_{1\rho}$-weighted MRI of tissues, image contrast is generated by molecular processes that occur at a range of frequencies determined by the amplitude of an applied spin-lock pulse. $T_{1\rho}$-weighted MRI has been performed on tissues such as brain, breast, and cartilage and has provided increased discrimination between normal and diseased tissue [1–7]. However, further improvements in signal-to-noise ratio (SNR) and resolution are possible with the use of surface coils. In particular, extremity joints such as the wrist and knee can be imaged with far greater SNR through the use of surface coils due to the proximity of the anatomical region of interest to the coil [8]. Signal enhancement with cryogenically cooled surface coils can also be employed to produce high-resolution ($<100\,\mu m$) images [9]. However, when transmitting with a surface coil, the inhomogeneous B_1 fields produces undesired image artifacts. Spatial variations in signal intensity arise from the complex rotations of off-axis magnetization vectors during the application of the radiofrequency (RF) pulses. There are no simple post-processing techniques to mitigate these errors and the resulting image is rendered useless for quantitative image analysis [10].

In this work, we present a pulse sequence to obtain $T_{1\rho}$-weighted MR images with a surface coil with image artifacts greatly reduced through the use of self-compensating spin-lock pulses [10]. Image artifacts generated by spin-locking pulses in the presence of inhomogeneous B_1 fields are simulated by solving the Bloch equations and are compared to experimental data for both the conventional and self-compensating $T_{1\rho}$ imaging sequences. Finally, after confirming that the RF deposition resulting from the new pulse sequence is within FDA mandated safety levels, the utility of the new pulse sequence for $T_{1\rho}$-weighted MRI on a clinical scanner is demonstrated in a phantom and in the knee-joint of a healthy human volunteer.

* Corresponding author. Fax: 1-215-573-2113.
E-mail address: ari@mail.mmrrcc.upenn.edu (A. Borthakur).

1090-7807/$ - see front matter © 2004 Elsevier Inc. All rights reserved.
doi:10.1016/j.jmr.2004.01.007

2. Theory

$T_{1\rho}$-weighted MRI can be performed with a variety of pulse sequences [6,11–14]. We designed a $T_{1\rho}$ MR imaging pulse sequence (Fig. 1) in which a three-pulse cluster prepares the magnetization before a 3D fast gradient-echo readout [15]. The three-pulse cluster contains a hard $\pi/2$-pulse that nutates the longitudinal magnetization into the transverse plane. Immediately following, a long duration, low-power pulse (labeled "SL") phase-shifted by 90° relative to the first pulse is applied to spin-lock the transverse magnetization. The second hard $\pi/2$, phase shifted by 180° from the first pulse, returns the spin-lock or $T_{1\rho}$-prepared magnetization back to the longitudinal axis. Finally, a strong crusher gradient is applied to destroy any residual transverse magnetization. The use of a preparatory pulse sequence permits imaging to be performed by simply appending any standard imaging sequence. It is important to note that the fast gradient-echo readout scheme employed in the current work imparts additional T_1-weighted image contrast.

Solving the Bloch equations for all on-resonant spins that experience the $\pi/2$ nutations, the expression for the $T_{1\rho}$-prepared magnetization at the end of the second hard $\pi/2$ pulse is:

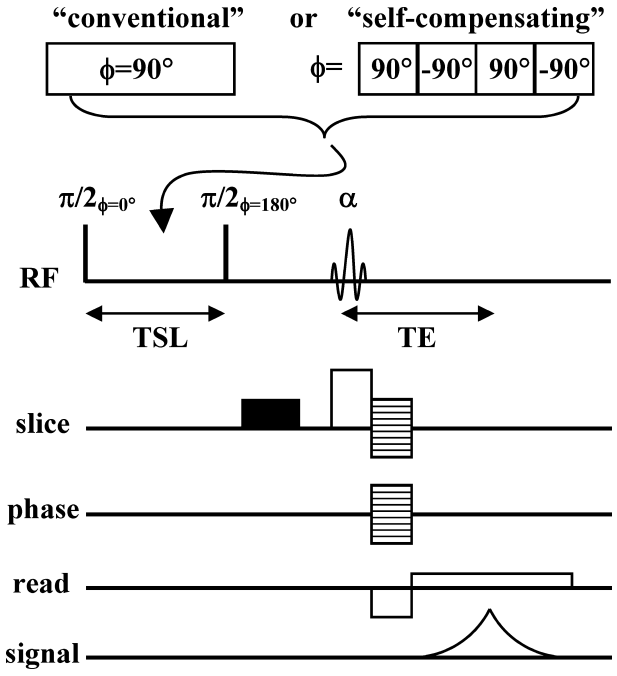

Fig. 1. Pulse sequence for $T_{1\rho}$-weighted MRI with a surface coil. The spin-lock pulse was either a single pulse with a constant phase and duration TSL ("conventional"), or divided into several segments with alternating phase and equal durations ("self-compensating"). A strong crusher gradient, shown as a solid block in the slice gradient axis, is applied to destroy any residual magnetization in the transverse plane. The $T_{1\rho}$-prepared longitudinal magnetization is then recalled and spatially encoded by any imaging sequence. In the current experiments, a 3D fast gradient-echo sequence was employed.

$$M_Z = M_0 e^{\frac{-TSL}{T_{1\rho}}}, \tag{1}$$

where M_0 is the longitudinal equilibrium magnetization and TSL is the duration of the spin-lock pulse.

Similarly, for arbitrary flip angles, the Bloch equation solution can be used to determine the magnetization at the end of the crusher gradient and immediately before the imaging pulse, α [10]. We assume that at the beginning of the pulse sequence, there is only a longitudinal component of the magnetization vector, M_0. If a hard RF pulse is applied on the system, the inhomogeneous RF field of a surface coil will produce a spatially varying B_1 field and hence not all spins will experience the same flip angle. Therefore, when using surface coils it is more appropriate to represent hard pulses as 'θ' pulses. At the end of the first θ pulse, (applied along the x-axis, i.e., phase $\phi = 0°$) we have the following components of magnetization:

$$\begin{aligned} \boldsymbol{M}_x &= 0, \\ \boldsymbol{M}_y &= M_0 \sin\theta, \\ \boldsymbol{M}_z &= M_0 \cos\theta. \end{aligned} \tag{2}$$

We then apply an SL pulse for a time TSL along the y-axis ($\phi = 90°$) and, for the time being, assume a constant phase for the spin-locking pulse. The component of magnetization perpendicular to the spin-lock B_1 rotates around B_1, while the component parallel to B_1 undergoes $T_{1\rho}$ relaxation. These processes produce the following magnetization components:

$$\begin{aligned} \boldsymbol{M}_x &= -M_0 e^{\frac{-TSL}{T_{2\rho}}} \cos\theta \sin\beta, \\ \boldsymbol{M}_y &= M_0 e^{\frac{-TSL}{T_{1\rho}}} \sin\theta, \\ \boldsymbol{M}_z &= M_0 e^{\frac{-TSL}{T_{2\rho}}} \cos\theta \cos\beta, \end{aligned} \tag{3}$$

where β is phase accumulation by off-axis spins (whose $\theta \neq \pi/2$) undergoing rotation during the spin-lock field. Therefore, $\beta = \gamma B_{SL} \cdot TSL$, where B_{SL} is the amplitude of the SL pulse and $T_{2\rho}$ is the time constant of decay of the magnetization perpendicular to a spin-locking field, which can be estimated as the reciprocal average of T_1 and T_2 [16].

The application of another $\theta(\phi = 180°)$ pulse will result in the vector components:

$$\begin{aligned} \boldsymbol{M}_x &= -M_0 e^{\frac{-TSL}{T_{2\rho}}} \cos\theta \sin\beta, \\ \boldsymbol{M}_y &= M_0 \left(e^{\frac{-TSL}{T_{1\rho}}} \sin\theta \cos\theta - e^{\frac{-TSL}{T_{2\rho}}} \cos\theta \cos\beta \sin\theta \right), \\ \boldsymbol{M}_z &= M_0 \left(e^{\frac{-TSL}{T_{2\rho}}} \cos\theta \cos\beta \cos\theta + e^{\frac{-TSL}{T_{1\rho}}} \sin\theta \sin\theta \right). \end{aligned} \tag{4}$$

A crusher gradient is then applied to destroy the transverse components leaving only the z-component:

$$\boldsymbol{M}_z = M_0 \left(e^{\frac{-TSL}{T_{2\rho}}} \cos^2\theta \cos\beta + e^{\frac{-TSL}{T_{1\rho}}} \sin^2\theta \right). \tag{5}$$

Eq. (5) is the general expression for the $T_{1\rho}$-prepared magnetization with 'θ' pulses and Eq. (1) is simply the special case when $\theta = \pi/2$. In practice, $T_{1\rho}$ images

obtained in an inhomogeneous B_1 field are marred with artifacts because θ and β exhibit spatial dependence, resulting in changes in M_Z. These artifacts are dependent on the duration and amplitude of the SL pulse, again because of the β parameter. Several strategies can be employed to reduce these artifacts. For example, adiabatic and composite RF pulses can be used to reduce errors resulting from frequency offsets and improper shimming [4,11,17,18]. In this work, however, a simpler method was employed in which the SL pulse was divided into even segments of equal duration with the phase of each segment alternating between $\pm 90°$, i.e., a "self-compensating" SL pulse [10]. Each SL pulse pair produces a rotary echo [16] and continuously refocuses the rotation experienced by the off-axis spins such that at the end of the pulse train the effective rotation angle β is zero. Further, segmenting the SL pulse in this manner introduces an additional T_2*-weighting during the "dead time" of the RF amplifier after the first hard $\pi/2$ pulse and after each SL pulse segment. Therefore, Eq. (5) must be modified to include an additional exponential term that is a function of T_2*, the dead time of the amplifier (T_d) and the number of SL segments (n). In the case where off-resonant spins arising from chemical-shifted species and inhomogeneities with MR linewidths are less than the SL frequency (500 Hz) and $T_d \ll T_2$*:

$$\boldsymbol{M}_z = M_0\left(e^{\frac{-TSL}{T_{2\rho}}}\cos^2\theta + e^{\frac{-(n+1)T_d}{T_2^*}}e^{\frac{-TSL}{T_{1\rho}}}\sin^2\theta\right). \quad (6)$$

For a complete derivation of this equation, please see the Appendix A. An additional exponential term containing the recovery of the longitudinal magnetization during the dead time could be included but its effect is negligible since $nT_d \ll T_1$ in the following experiments, and it is therefore ignored in the analysis.

3. Materials and methods

All MR experiments were performed on a 4 T GE clinical MRI system. $T_{1\rho}$-weighted images of a cylindrical (7 cm diameter and 12 cm long) agarose gel (4% w/v) phantom and a knee-joint of a 30-year-old healthy male volunteer were obtained with a custom-built surface coil (7 cm inner-diameter). The IRB committee of the University of Pennsylvania granted approval for the study and informed consent was obtained from the volunteer. All images were transferred to an Apple G4 titanium computer (Apple Computer, Cupertino, CA) and displayed with custom-written software in the IDL programming language (RSI, Boulder, CO).

3.1. RF pulse calibration

The hard pulses were nominally calibrated by first turning off the spin-lock and second hard pulses. The transmit gain of the first hard pulse was titrated while observing a one-dimensional image profile of the agarose gel phantom. Since the crusher gradient destroys transverse magnetization, a minimum in the image profile was attained when the hard pulse achieved a nominal 90° flip angle for a volume of interest in the coil. The transmit gain was fixed at this value for the rest of the experiments.

3.2. B_1 Mapping

The B_1 profile of the surface coil was calculated according to the method described by Insko and Bolinger [19]. The surface coil was centered on an agarose gel phantom (Fig. 2B). Two coronal images were acquired using a 2D gradient echo sequence with nominal flip angles of 10° and 20°, respectively. The choice of small flip angles prevented any over-flipping (i.e., flip angle greater than 90°) of spins in the imaged area. Other imaging parameters were TE/TR = 7/4000 ms, FOV = 10 cm × 10 cm, slice thickness of 3 mm, and a matrix size of 256 × 128. A long TR was employed to minimize any T_1 relaxation-dependent contrast.

The B_1 profile of the surface coil is given by [19]:

$$B_1 = \frac{1}{\gamma\tau}\cos^{-1}\left(\frac{1}{2r}\right). \quad (7)$$

In this equation, γ is the gyromagnetic ratio of proton and τ is the pulse width of the RF and r is the ratio of the signals from two fully relaxed gradient echo images with flip angles θ_1 and θ_2 and is given by:

$$r = \frac{\sin\theta_1}{\sin\theta_2}. \quad (8)$$

By choosing flip angles such that $\theta_2 = 2\theta_1$, the equation reduces to:

$$r = \frac{1}{2\cos\theta_1}. \quad (9)$$

Knowing $\theta_1 = \gamma B_1 \tau$ leads to the solution for B_1.

3.3. $T_{1\rho}$ Imaging

In the experiments using the self-compensating spin-lock pulse, either two or four spin-lock pulses with alternating phase were used with the durations of either 10 or 1 ms, respectively. Consequently, the TSL times were 20 and 4 ms. For comparison, single-phase ($\phi = 90°$) SL pulses of duration 20 ms and 4 ms were used in the conventional sequence. The amplitude of the SL pulse was fixed at 500 Hz for all phantom experiments but for time-efficiency and SAR considerations, the SL amplitude was set at 400 Hz for the in vivo experiments. The $T_{1\rho}$-prepared magnetization was sampled using a 3D fast gradient-echo imaging sequence with the following imaging parameters: TE/TR = 2.2/138 ms, FOV = 10 cm × 10 cm, 3 mm slice thickness, with

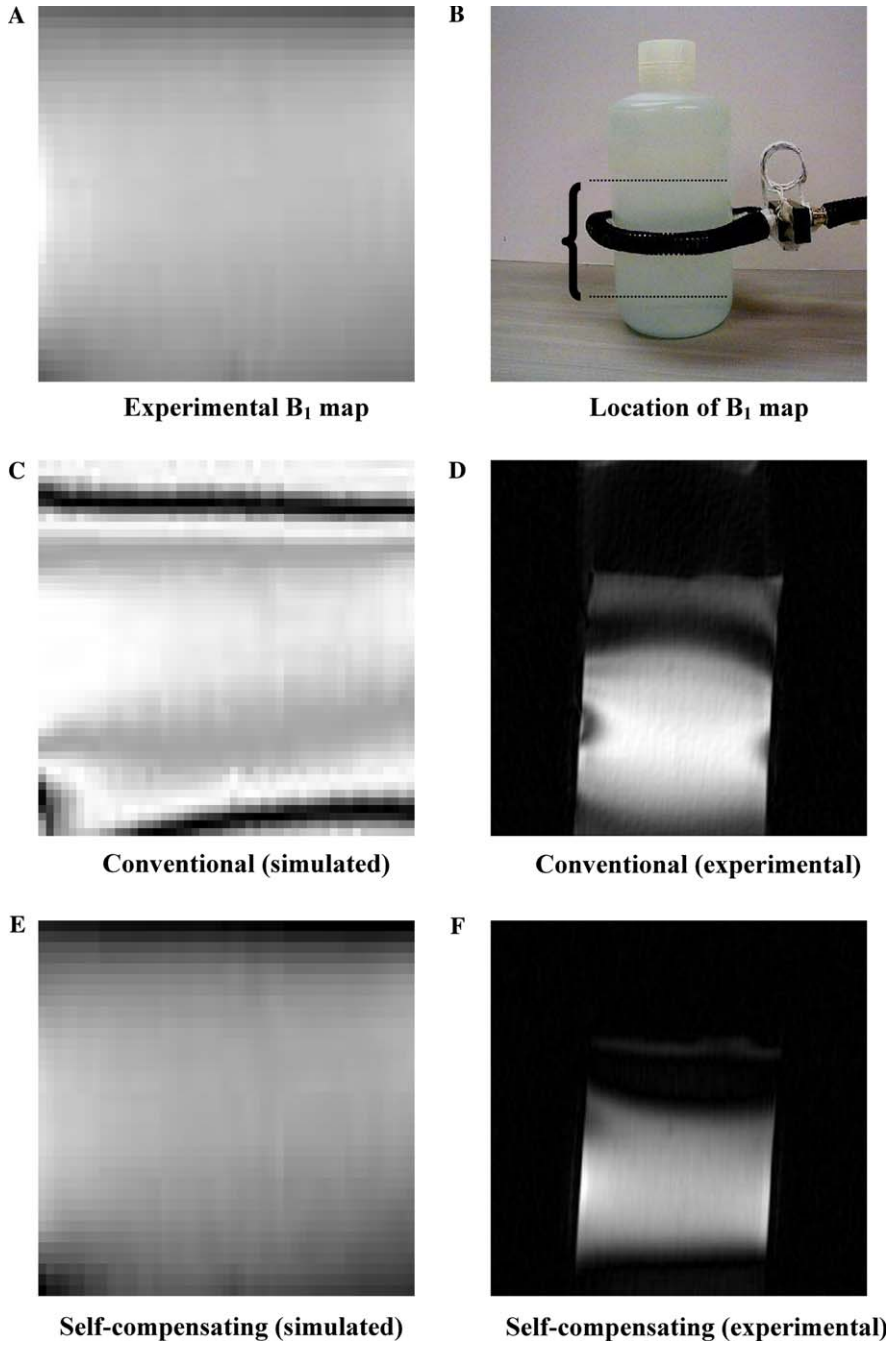

Fig. 2. An experimentally obtained B_1 map (A) in a plane perpendicular to the plane of the coil bounded by the region indicated in the photo of the phantom and surface coil set-up (B). The use of the conventional sequence produced artifacts in the simulated image (C), as well as in the $T_{1\rho}$ image of the phantom (D). This inhomogeneous signal distribution results from phase accumulation by off-axis spins during the application of the spin-lock pulse (i.e., $\beta \neq 0$ in Eq. (6)). Consequently, the self-compensating spin-lock pulse sequence reduced the artifacts in both the simulated image (E) as well as in the $T_{1\rho}$ image (F). Image D was obtained with one SL pulse of 4 ms duration and image F was obtained with two pulses of 2 ms each and alternating phases.

256×128 matrix size, and $\alpha = 30°$. The total imaging time was under 5 min for a data set of 16 slices. $T_{1\rho}$ relaxation time maps were generated by imaging the agarose gel phantom with five different TSL times ranging from 10 to 50 ms. Images were obtained with both the self-compensating sequence (using the surface coil) and with the conventional sequence using a 10-cm diameter birdcage volume coil. $T_{1\rho}$ maps were calculated by fitting image signal intensity for each pixel to the appropriate 3D $T_{1\rho}$ signal expression assuming a previously calculated T_1 of 1 s for the homogeneous phantom [15].

3.4. Simulations

The effect of an inhomogeneous B_1 field on the $T_{1\rho}$-weighted MR signal was simulated using Eq. (6). Simulated images of a theoretical cylindrical sample were generated with the experimentally determined B_1 map of the surface coil. The effects of both the conventional and self-compensating pulse sequences were investigated with identical imaging parameters as those of the imaging experiments. In addition, the self-compensating sequence employed multiple RF pulses with a hardware-limited dead time of 320 μs between each pulse. Its effect on the $T_{1\rho}$-prepared signal as a function of the number of SL segments was investigated by plotting the signal profile along an imaginary line through the center and perpendicular to the plane of the surface coil. From previous measurements on the agarose gel phantom, a homogeneous distribution of $T_{1\rho}$, $T_{2\rho}$ (equal to 50 and 30 ms, respectively) and T_2* (30 ms) was assumed for the entire sample.

3.5. SAR calculation and temperature mapping

Care was taken to ensure that the RF power deposited during in vivo $T_{1\rho}$ imaging remained below FDA mandated safety levels for the specific absorption rate, or SAR [20]. In addition to monitoring RF power levels with a meter connected in series with the coil, the SAR was calculated from the electric field on a simulated phantom of known tissue electrical properties and material density using a method proposed by Collins et al. [21]. As this model assumes that the electric field is generated by a quadrature bird-cage head coil, we further measured the actual temperature increase produced by the surface coil in a phantom using a previously validated temperature mapping technique [22]. In this method, MR phase images of a 10 cm-diameter, disc-shaped 160 mM $CoCl_2$-doped agarose gel (4% w/v) phantom weighing 1 kg are acquired before (pre-test) and after (post-test) running a "test" pulse sequence to heat the phantom, which in our case, was the 3D $T_{1\rho}$-weighted pulse sequence with and without the self-compensating SL pulses. For a fixed SL pulse amplitude and TSL time, a minimum allowable TR for the $T_{1\rho}$ sequence was calculated to ensure compliance with safe SAR levels. Other pulse sequence parameters for $T_{1\rho}$ imaging were FOV = 10 cm × 10 cm, 3 mm slice thickness, with 256 × 128 matrix size, and $\alpha = 30°$. The pre- and post-test data sets were acquired by a 2D multi-slice gradient echo sequence with FOV = 15 cm × 15 cm, slice thickness = 3 mm, TE/TR = 20/500 ms and a data matrix of 256 × 128 pixels. The phase difference between the pre-test and post-test images resulting from the temperature-dependent chemical shift of the water peak was used to generate phase-difference maps that were directly converted to temperature maps to visualize any regions of excessive (> 0.1 °C) heating. The power meter reading and total imaging time were also used to calculate an expected temperature rise, with the assumption that all RF power was converted to heat in the phantom and that the specific heat of the 4% agarose gel was that of pure water, 4.18 J/g/K. These experiments and simulations helped optimize the imaging parameters for in vivo imaging, which were TE/TR = 2.2/138 ms, FOV = 10 cm × 10 cm, 3 mm slice thickness, with 256 × 128 matrix size, and $\alpha = 30°$. The amplitude of the SL pulse was fixed at 400 Hz and TSL was 10 ms.

4. Results

Results from the simulated and experimental data obtained on a phantom are shown in Fig. 2. The experimentally obtained B_1 profile through a center slice, perpendicular to the plane of a surface coil is shown (A). As expected, there is a drop-off in B_1 away from the center of the coil element. When the conventional sequence is performed in the presence of this B_1 profile, bands of low signal intensities are visible in the simulated image (C). Inhomogeneities in B_1 generate a complicated cosine modulated signal profile along the direction of the B_1 gradient resulting in artifacts that degrade image quality. We have previously shown that the amplitude of these oscillations depends on $T_{2\rho}$, with a short $T_{2\rho}$ producing oscillations with lower

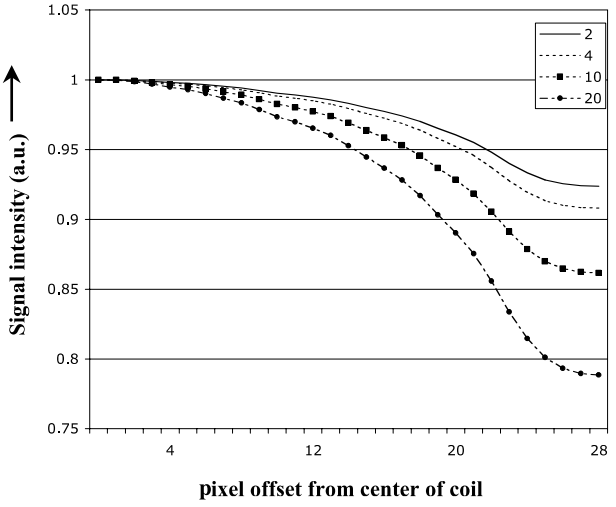

Fig. 3. The effect of number of spin-lock segments employed in the self-compensating pulse sequence on the signal profile across a simulated phantom of homogeneous $T_{1\rho}$ (50 ms). Employing two RF pulses of 2 ms each produced a signal drop-off (solid line) in regions away from the coil. The rate of this signal drop-off increased with greater number of RF pulses (4, 10 or 20 alternating-phase RF pulse trains). The B_1 map from Fig. 2A was assumed and the position of the surface coil corresponds to a vertical line through the zero of the abscissa.

amplitude, while the overall signal intensity is determined by the component of the magnetization that was spin-locked and is therefore dependent on $T_{1\rho}$ [10]. An experimental $T_{1\rho}$-weighted MR image of the agarose phantom also shows similar artifacts (D). However, when the self-compensating pulse sequence was employed, the artifacts vanished from both the simulated (E) and the $T_{1\rho}$-weighted images (F) of the phantom. In contrast, the conventional sequence utilizes a single SL pulse with $\phi = 90°$ so that $\beta \neq 0$ and artifacts are produced as a result.

The self-compensating scheme utilized multiple spin-lock pulses and the dead time between these pulses leads to signal attenuation that scaled with the number of RF pulses. This was shown quite readily in the simulations, where, as the same TSL time was sub-divided into a larger number of phase-alternating RF pulses, the signal diminished more rapidly in regions away from the center of the coil (Fig. 3). It is evident from Eq. (6) that the MR signal would depend not only on the B_1 profile of the coil but also on the T_2* decay experienced by spins during time T_d and the number of spin-lock segments. Regions with low B_1 experienced smaller flip angles, and therefore had smaller components of magnetization that could experience spin-locking. Since T_2* is always less than $T_{1\rho}$, the signal decay is more pronounced in regions that experienced smaller flip angles than in regions closer to the coil.

The effect of increasing TSL times was demonstrated in images of the phantom obtained in the plane of the surface coil (Fig. 4). The longer TSL images (B,D) have more image distortions in both sequences compared to their respective short TSL images (A,C) since any imperfections in B_1 will result in image artifacts and, as Eq. (6)

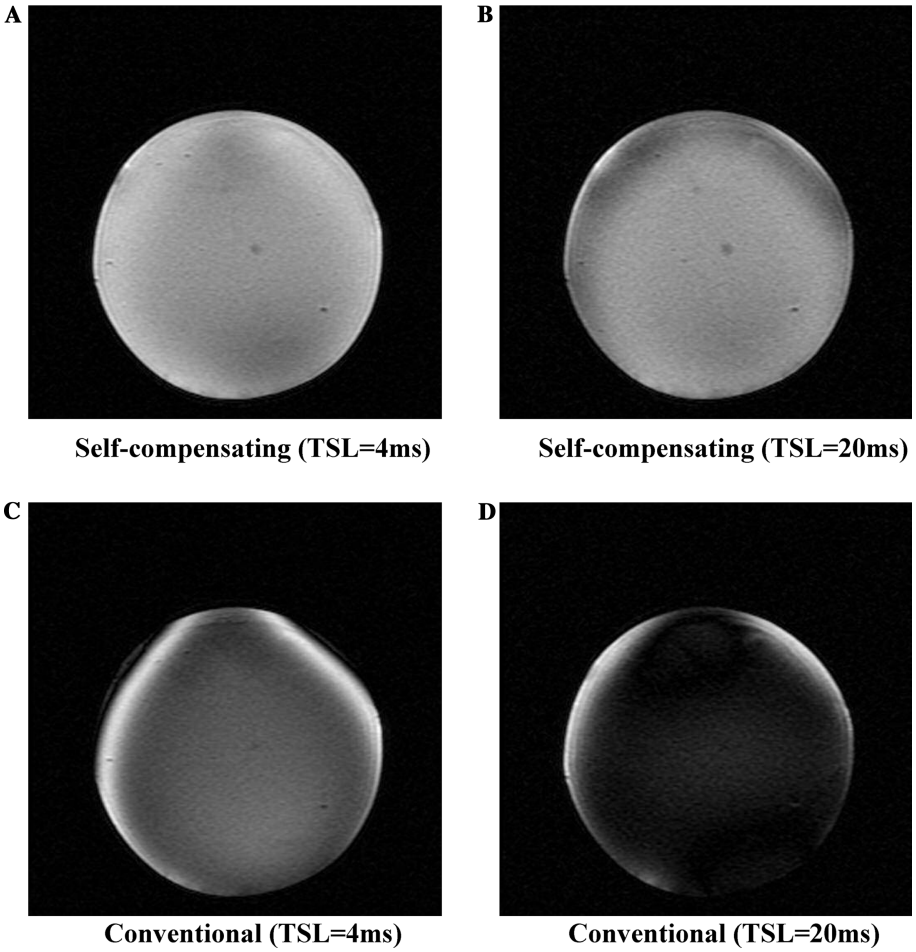

Fig. 4. $T_{1\rho}$-weighted MR images of the agarose gel phantom obtained with the self-compensating (A,B) and the conventional (C,D) methods. The images are in the plane of the surface coil. In A, the SL pulse is divided into 4 segments of 1 ms each (i.e., TSL = 4 ms) and in B is divided into two segments of 10 ms each (i.e., TSL = 20 ms). For comparison, image C was obtained with a single SL pulse of constant phase and 4 ms duration and image D was obtained with a single SL pulse of constant phase and 20 ms duration. The self-compensating scheme performs optimally at smaller TSL times (A) and image distortions begin to appear at longer TSL times (B). At the same time, regardless of the TSL time, the self-compensated images (A,B) contain fewer distortions than the corresponding conventional images (C,D).

suggests, the phase accumulation will propagate linearly with TSL time. At the same time, however, the self-compensated images (A,B) showed far fewer distortions than their corresponding images obtained with the conventional sequence (C,D). $T_{1\rho}$ mapping experiments demonstrated that the self-compensating sequence using a surface coil produces similar $T_{1\rho}$ values as that obtained with conventional sequence using a volume coil (Fig. 5).

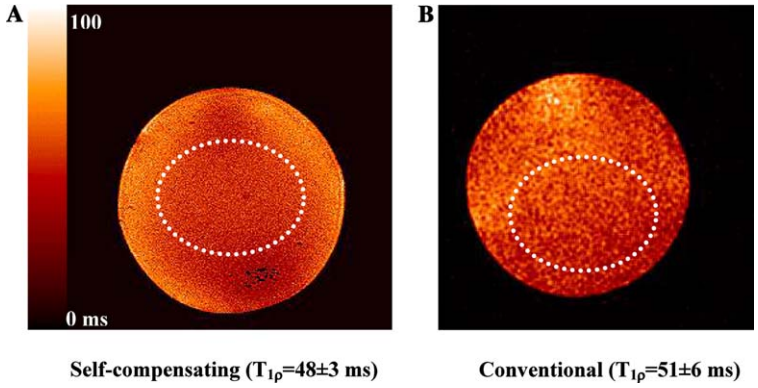

Fig. 5. $T_{1\rho}$ maps of the same agarose gel phantom from Fig. 4 generated by fitting images obtained with the self-compensating sequence using a surface coil (A) and with the conventional sequence using a volume bird-cage coil (B). The maps are windowed from $T_{1\rho}$ values of zero to a 100 ms as indicated by the color bar on the left. Average (±SD) using both methods resulted in similar $T_{1\rho}$ values in the regions of interest enclosed by the dotted ovals on both images. As expected, identical imaging parameters resulted in a difference in image quality due to the higher SNR of the surface coil experiments.

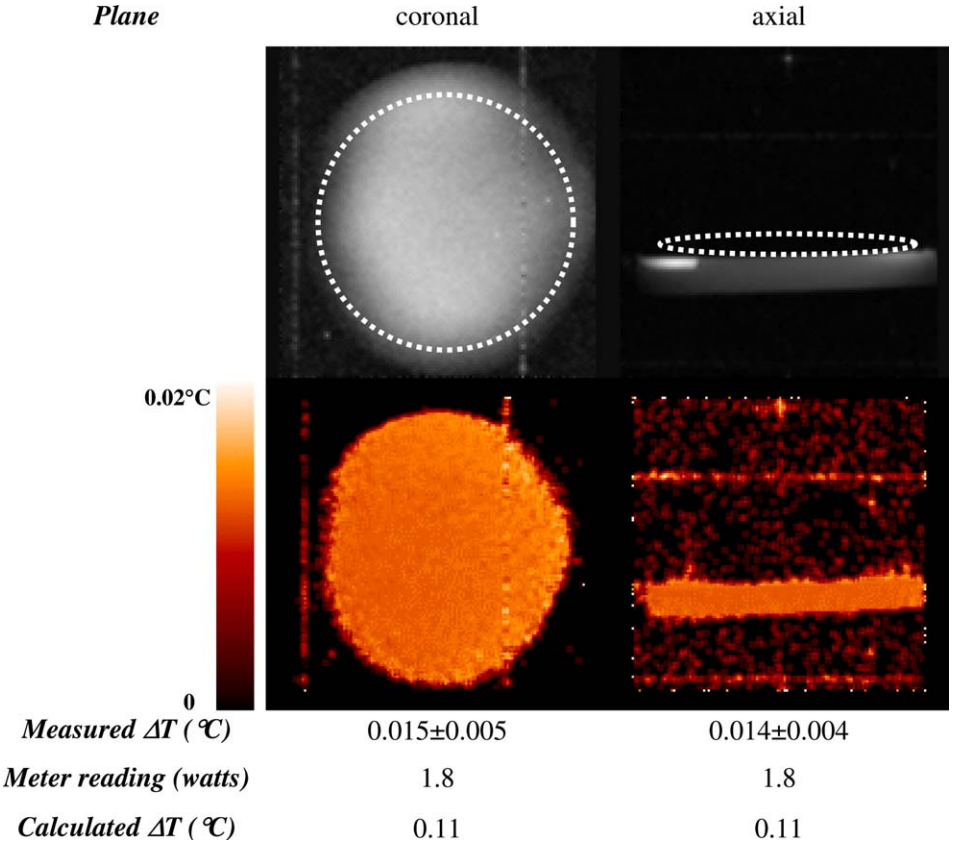

Fig. 6. Data from temperature mapping experiments on the agarose gel phantom. Representative image and temperature map resulting from RF heating during the 3D $T_{1\rho}$ MRI with a surface coil in a coronal plane adjacent to the coil and axial plane through the middle of the phantom. The temperature rise in the phantom calculated from the temperature maps is less than 0.016 °C, indicating that there was no significant heating. The power meter reading was the same in both image data sets as they were "heated" using the same imaging sequence. The calculated (or "worst-case") temperature rise if all the power from the coil went into heating the sample was an order of magnitude higher (0.1 °C).

The minimum TR was limited to 138 ms for the in vivo experiments after verifying the SAR of the new pulse-sequence through power meter reading and calculations. This value of TR guaranteed a safe duty cycle for RF deposition to the tissue and minimized the total imaging time. This was further verified by temperature mapping, representative data from which is shown in Fig. 6. The first image in column A is a $T_{1\rho}$-weighted image of the phantom in the coronal plan with a dotted circle showing the location of the surface coil. The color image below this shows the temperature map generated after running the test $T_{1\rho}$ 3D sequence for 5 min. An axial image through the middle of the disc-shaped phantom (Fig. 6 column B) shows regions of increased signal intensity close to the wire of the surface coil (the plane of which is indicated by the dotted line). The measured average temperature rise was less than 0.016 °C and there were no regions of excessive heating in either plane. The calculated temperature rise expected if all the power from the surface coil went into heating the phantom was an order of magnitude higher (0.1 °C). This overestimation of calculated temperature rise is expected as it was assumed, in the rather simplistic calculation of the "worst-case" scenario, that there were no mechanisms of heat loss from the phantom during the experiments and all of the power from the RF coil was converted into heating the phantom.

Two representative slices are shown from the 3D data set of $T_{1\rho}$-weighted images of the knee joint with a surface coil in vivo (Fig. 7). The advantage of employing self-compensated spin-locking pulses is clearly evident in both images in the left column. Use of conventional spin-locking (right column) generated bands of inhomogeneous signal intensity visible across the cartilage tissue between the patella and distal femur, rendering

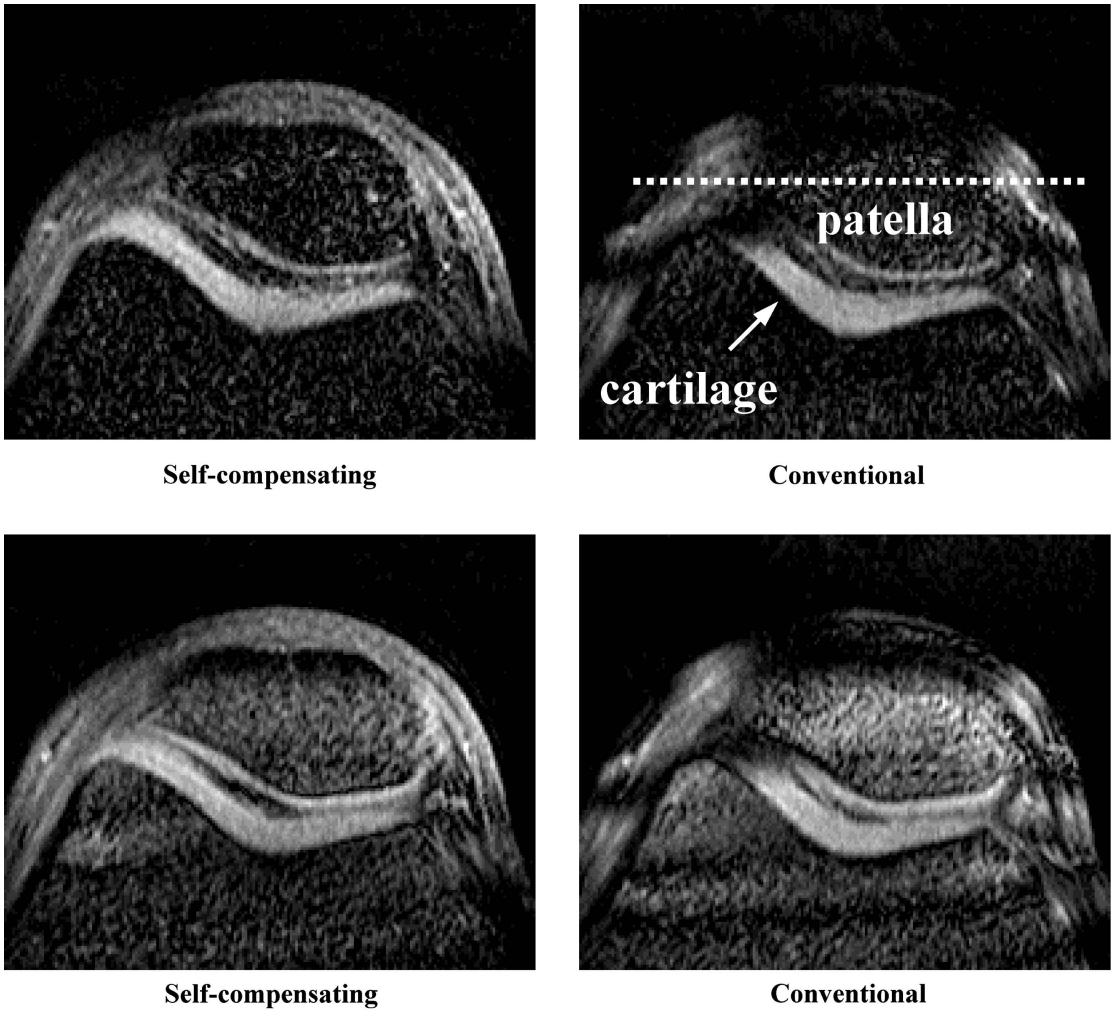

Fig. 7. In vivo $T_{1\rho}$-weighted axial MR images of the human knee joint obtained with a surface coil with the self-compensating and conventional pulse sequences. Severe artifacts are visible in both images obtained with the conventional sequence particularly in the regions of the patella and surrounding cartilage. The reduction of these artifacts is clearly appreciable in the self-compensated images (dotted line indicates the location of the plane of the surface coil during image acquisition).

the images useless for quantitative analysis. The self-compensated images contain far fewer artifacts in the same region.

5. Discussion

Quantitative $T_{1\rho}$ MRI experiments have been utilized to calculate spatial distribution of $T_{1\rho}$ values, a technique commonly referred to as "$T_{1\rho}$-mapping," where$T_{1\rho}$ values are calculated on a pixel-by-pixel basis by fitting data (to Eq. (1)) from multiple images with increasing TSL times [23,24]. In the setting of an inhomogeneous B_1 field, conventional spin-locking generates multiple image artifacts, which vary with TSL, thereby preventing $T_{1\rho}$ mapping. The use of self-compensating spin-locking reduces these artifacts and facilitates quantitative relaxation time measurement. However, care must be taken when employing the surface coil imaging technique described in this work to determine $T_{1\rho}$ maps. The reason for this is as follows. $T_{1\rho}$ is a quantity that varies with the amplitude of the applied spin-lock field, a property termed $T_{1\rho}$ dispersion. Therefore, even if artifacts are removed, a spatially varying B_1 (as would occur with a surface coil) results in a spatially varying $T_{1\rho}$. This phenomenon may generate image contrast that arises from properties of the B_1 field rather than properties of the tissue of interest. Of course, the variation of $T_{1\rho}$ with B_1 is typically rather slow, and it may be possible to overcome $T_{1\rho}$ dispersion effects by achieving a relatively homogeneous B_1 in a particular sensitive volume of the surface coil as the results in Fig. 5 demonstrate. Alternatively, one might obtain a B_1 map of the surface coil and use this to determine $T_{1\rho}$ as a function of B_1 at every pixel in the image. Another potential limitation of this technique to correct artifacts arises when there is significant motion of spins in the inhomogeneous B_1 field of the surface coil. Moving spins will not be adequately re-phased by the alternating phase spin-lock segments and the resulting phase accumulation would lead to persistent image artifacts. In addition, off-resonant spins arising from chemical-shifted species and inhomogeneities with MR linewidths greater than the SL frequency (500 Hz) will not be re-phased by the self-compensating SL pulse train. In such cases, the spin-locking vector will be situated at an angle to the transverse plane and negating its phase will only change the direction of the vector's transverse component so that it maintains its angle to the transverse plane and self-compensation is ineffective.

In conclusion, a new self-compensating spin-lock pulse sequence that allows $T_{1\rho}$-MRI with surface coils was implemented on a clinical scanner. Simulated $T_{1\rho}$ images were generated using the theoretical signal expressions for both the self-compensating and conventional spin-locking strategies in the presence of an inhomogeneous B_1 field. The sequence was also tested on a phantom and in the human knee joint in vivo. A reduction in image artifacts was observed using the new pulse sequence in the simulated data as well as in the phantom and in vivo data. Further work is under way to optimize additional imaging parameters such as TSL and number of spin-lock segments in the pulse sequence. In addition, the potential utility of this pulse sequence for $T_{1\rho}$ mapping is under evaluation.

Acknowledgments

This work was performed at a NIH supported resource center (NIH RR02305) and supported by Grants R01-AR45242 and R01-AR45404 from National Institutes of Arthritis, Musculoskeletal, and Skin Diseases (NIAMS). We thank Professor John S. Leigh for his encouragement and support.

Appendix A

The derivation of Eq. (6) under off-resonance conditions is shown here. We begin by assuming the following pulse sequence, containing only a pair of SL segments, however, the final equation can easily be generalized for multiple SL pairs:

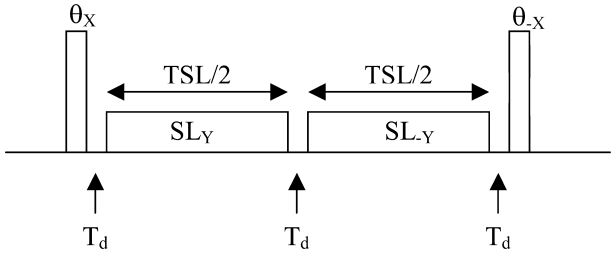

Starting with magnetization $Iz : Iz \rightarrow \theta x \rightarrow Iz\cos\theta + Iy\sin\theta$.

Under off-resonance ($\Delta\omega$) and T_2^* relaxation during T_d time period, we get:

$$Iz\cos\theta + Iy\sin\theta\cos\Delta\omega T_d\exp(-T_d/T_2^*) + Ix\sin\theta\sin\Delta\omega T_d\exp(-T_d/T_2^*).$$

Simplify to:

$$Iz\cos\theta + Iy\sin\theta\partial 1 + Ix\sin\theta\partial 2.$$

Effect of first SL pulse applied along y-axis and assuming that the linewidth of inhomogeneities is less than the SL frequency (500 Hz), i.e., no $\Delta\omega$ terms during spin-lock pulse, we get:

$$Iy\sin\theta\partial 1\exp(-\mathrm{TSL}/2T_{1\rho}) + \{\cos\theta[Iz\cos\beta - Ix\sin\beta] + \sin\theta\partial 2[Iz\sin\beta + Ix\cos\beta]\}\exp(-\mathrm{TSL}/2T_{2\rho}),$$

where $\beta = \gamma B_{\mathrm{SL}}\cdot \mathrm{TSL}/2$, and B_{SL} is the amplitude of the SL pulse and $T_{2\rho}$ is the decay rate of the magnetization perpendicular to a spin-locking field.

Collect like terms:

$$Iy\sin\theta\partial 1\exp(-\mathrm{TSL}/2T_{1\rho}) + Ix[\sin\theta\cos\beta\partial 2 - \cos\theta\sin\beta]\exp(-\mathrm{TSL}/2T_{2\rho}) + Iz[\cos\theta\cos\beta + \sin\theta\sin\beta\partial 2]\exp(-\mathrm{TSL}/2T_{2\rho}).$$

Simplify to:

$$Ix\mathbf{A1} + Iy\mathbf{A2} + Iz\mathbf{A3}.$$

During second T_{d} time period, we get:

$$IzA3 + [A2(Iy\cos\Delta\omega T_{\mathrm{d}} + Ix\sin\Delta\omega T_{\mathrm{d}}) + A1(Ix\cos\Delta\omega T_{\mathrm{d}} - Iy\sin\Delta\omega T_{\mathrm{d}})]\exp(-T_{\mathrm{d}}/T_2^*).$$

Collect like terms:

$$IzA3 + Iy(A2\cos\Delta\omega T_{\mathrm{d}} - A1\sin\Delta\omega T_{\mathrm{d}})\exp(-T_{\mathrm{d}}/T_2^*) + Ix(A2\sin\Delta\omega T_{\mathrm{d}} + A1\cos\Delta\omega T_{\mathrm{d}})\exp(-T_{\mathrm{d}}/T_2^*).$$

Simplify to

$$Ix\mathbf{B1} + Iy\mathbf{B2} + IzA3.$$

Effect of second SL pulse applied along $-y$-axis:

$$IyB2\exp(-\mathrm{TSL}/2T_{1\rho}) + A3[\cos(-\beta) - Ix\sin(-\beta)]\exp(-\mathrm{TSL}/2T_{2\rho}) + B1[Ix\cos(-\beta) + Iz\sin(-\beta)]\exp(-\mathrm{TSL}/2T_{2\rho}).$$

Collect like terms:

$$Ix[-A3\sin(-\beta) + B1cos(-\beta)]\exp(-\mathrm{TSL}/2T_{2\rho}) + IyB2\exp(-\mathrm{TSL}/2T_{1\rho}) + Iz[A3\cos(-\beta) + B1\sin(-\beta)]\exp(-\mathrm{TSL}/2T_{2\rho}).$$

Simplify to:

$$Ix\mathbf{C1} + Iy\mathbf{C2} + Iz\mathbf{C3}.$$

During last T_{d} time period, we get:

$$IzC3 + [C2(Iy\cos\Delta\omega T_{\mathrm{d}} + Ix\sin\Delta\omega T_{\mathrm{d}}) + C1(Ix\cos\Delta\omega T_{\mathrm{d}} - Iy\sin\Delta\omega T_{\mathrm{d}})]\exp(-T_{\mathrm{d}}/T_2^*).$$

Collect like terms:

$$IzC3 + Iy(C2\cos\Delta\omega T_{\mathrm{d}} - C1\sin\Delta\omega T_{\mathrm{d}})\exp(-T_{\mathrm{d}}/T_2^*) + Ix(C2\sin\Delta\omega T_{\mathrm{d}} + C1\cos\Delta\omega T_{\mathrm{d}})\exp(-T_{\mathrm{d}}/T_2^*).$$

Simplify to:

$$Ix\mathbf{D1} + Iy\mathbf{D2} + IzC3.$$

Finally, the θ along $-x$ axis followed by a crusher gradient will leave only the z component:

$$Iz[C3\cos(-\theta) - D2\sin(-\theta)].$$

For small frequency offsets and delay times, $\Delta\omega T_{\mathrm{d}} \sim 0 \Rightarrow \partial 2 = 0$ and $\partial 1 = \exp(-T_{\mathrm{d}}/T_2^*)$. The expression can then be simplified to:

$$Iz[C3\cos\theta + C2\exp(-T_{\mathrm{d}}/T_2^*)\sin\theta].$$

Therefore,

$$M_Z = M_0\{\exp(-\mathrm{TSL}/T_{2\rho})\cos^2\theta \times [\cos^2\beta + \sin^2\beta\exp(-T_{\mathrm{d}}/T_2^*)] + \exp(-3T_{\mathrm{d}}/T_2^*)\exp(-\mathrm{TSL}/T_{1\rho})\sin^2\theta\}.$$

For the simulations, we assumed a T_2^* of 30 ms and a T_{d} of 320 μs, so that this expression simplifies to Eq. (6).

References

[1] A.E. Lamminen, J.I. Tanttu, R.E. Sepponen, H. Pihko, O.A. Korhola, $T_{1\rho}$ dispersion imaging of diseased muscle tissue, Br. J. Radiol. 66 (1993) 783–787.

[2] G.E. Santyr, MR imaging of the breast. Imaging and tissue characterization without intravenous contrast, Magn. Reson. Imaging Clin. N Am. 2 (1994) 673–690.

[3] A.T. Markkola, H.J. Aronen, T. Paavonen, E. Hopsu, L.M. Sipila, J.I. Tanttu, R.E. Sepponen, Spin lock and magnetization transfer imaging of head and neck tumors, Radiology 200 (1996) 369–375.

[4] W.T. Dixon, J.N. Oshinski, J.D. Trudeau, B.C. Arnold, R.I. Pettigrew, Myocardial suppression in vivo by spin locking with composite pulses, Magn. Reson. Med. 36 (1996) 90–94.

[5] A. Virta, M. Komu, N. Lundbom, M. Kormano, T1rho MR imaging characteristics of human anterior tibial and gastrocnemius muscles, Acad. Radiol. 5 (1998) 104–110.

[6] H.J. Aronen, U.A. Ramadan, T.K. Peltonen, A.T. Markkola, J.I. Tanttu, J. Jaaskelainen, A.M. Hakkinen, R. Sepponen, 3D spin-lock imaging of human gliomas, Magn. Reson. Imaging 17 (1999) 1001–1010.

[7] U. Duvvuri, S.R. Charagundla, S.B. Kudchodkar, J.H. Kaufman, J.B. Kneeland, R. Rizi, J.S. Leigh, R. Reddy, Human knee: in vivo T1(rho)-weighted MR imaging at 1.5 T—preliminary experience, Radiology 220 (2001) 822–826.

[8] J.S. Yu, Magnetic resonance imaging of the wrist, Orthopedics (Thorofare, NJ) 17 (1994) 1041–1048.

[9] A.C. Wright, H.K. Song, F.W. Wehrli, In vivo MR micro imaging with conventional radiofrequency coils cooled to 77 K, Magn. Reson. Med. 43 (2000) 163–169.

[10] S.R. Charagundla, A. Borthakur, J.S. Leigh, R. Reddy, Artifacts in T1[rho]-weighted imaging: correction with a self-compensating spin-locking pulse, J. Magn. Reson. 162 (2003) 113–121.

[11] R.E. Sepponen, J.A. Pohjonen, J.T. Sipponen, J.I. Tanttu, A method for $T_{1\rho}$ imaging, J. Comput. Assist. Tomogr. 9 (1985) 1007–1011.

[12] R.V. Mulkern, S. Patz, M. Brooks, D.C. Metcalf, F.A. Jolesz, Spin-lock techniques and CPMG imaging sequences: a critical appraisal of T1ρ contrast at 0.15 T, Magn. Reson. Imaging 7 (1989) 437–444.

[13] G.E. Santyr, R.M. Henkelman, M.J. Bronskill, Spin locking for magnetic resonance imaging with application to human breast, Magn. Reson. Med. 12 (1989) 25–37.

[14] R.R. Rizi, S.R. Charagundla, H.K. Song, R. Reddy, A.H. Stolpen, M.D. Schnall, J.S. Leigh, Proton $T_{1\rho}$-dispersion imaging of rodent brain at 1.9 T, J. Magn. Reson. Imaging 8 (1998) 1090–1096.

[15] A. Borthakur, A.J. Wheaton, S.R. Charagundla, E.M. Shapiro, R.R. Regatte, S.V.S. Akella, J.B. Kneeland, R. Reddy, Three-dimensional $T1\rho$-weighted MRI at 1.5 Tesla, J. Magn. Reson. Imaging 17 (2003) 730–736.
[16] I. Solomon, Rotary spin echoes, Phys. Rev. Lett. 2 (1959) 301–302.
[17] A. Tannus, M. Garwood, Adiabatic pulses, NMR Biomed. 10 (1997) 423–434.
[18] A. Virta, M. Komu, N. Lundbom, S. Jaaskelainen, H. Kalimo, A. Airio, A. Alanen, M. Kormano, Low field T1rho imaging of myositis, Magn. Reson. Imaging 16 (1998) 385–391.
[19] E.K. Insko, L. Bolinger, Mapping of the radiofrequency field, J. Magn. Reson. Series A 103 (1993) 82–85.
[20] US Food & Drug Administration. 1998 Nov 14. Guidance for the submission of premarket notifications for magnetic resonance diagnostic devices. Available from http://www.fda.gov/cdrh/ode/mri340.pdf. Accessed 2002 Jul 18.
[21] C.M. Collins, S. Li, M.B. Smith, SAR and B_1 field distributions in a heterogeneous human head model within a birdcage coil, Magn. Reson. Med. 40 (1998) 847–856.
[22] E.M. Shapiro, A. Borthakur, M.J. Shapiro, R. Reddy, J.S. Leigh, Fast MRI of RF heating via phase difference mapping, Magn. Reson. Med. 47 (2002) 492–498.
[23] S.V. Akella, R. Reddy Regatte, A.J. Gougoutas, A. Borthakur, E.M. Shapiro, J.B. Kneeland, J.S. Leigh, R. Reddy, Proteoglycan induced changes in $T_{1\rho}$-relaxation of articular cartilage at 4 T, Magn. Reson. Med. 46 (2001) 419–423.
[24] D.R. Tailor, A. Roy, R.R. Regatte, S.R. Charagundla, A.C. McLaughlin, J.S. Leigh, R. Reddy, Indirect 17O-magnetic resonance imaging of cerebral blood flow in the rat, Magn. Reson. Med. 49 (2003) 479–487.